Illustrative view on the magnetocrystalline anisotropy of adatoms and monolayers

O. Šipr,[1,*] S. Mankovsky,[2] S. Polesya,[2] S. Bornemann,[2] J. Minár,[2,3] and H. Ebert[2]
[1]*Institute of Physics ASCR v. v. i., Cukrovarnická 10, CZ-162 53 Prague, Czech Republic*
[2]*Universität München, Department Chemie, Butenandtstrasse 5-13, D-81377 München, Germany*
[3]*New Technologies Research Centre, University of West Bohemia, Pilsen, Czech Republic*
(Received 17 March 2016; revised manuscript received 20 April 2016; published 13 May 2016)

Although it has been known for decades that magnetocrystalline anisotropy is linked to spin-orbit coupling (SOC), the mechanism of how it arises for specific systems is still a subject of debate. We focused on finding markers of SOC in the density of states (DOS) and on using them to understand the source of magnetocrystalline anisotropy for the case of adatoms and monolayers. Fully relativistic *ab initio* Korringa-Kohn-Rostoker Green's-function calculations were performed for Fe, Co, and Ni adatoms and monolayers on Au(111) to investigate changes in the orbital-resolved DOS due to a rotation of magnetization. In this way, one can see that a significant contribution to magnetocrystalline anisotropy for adatoms comes from pushing the SOC-split states above or below the Fermi level. As a result of this, the magnetocrystalline anisotropy energy depends crucially on the position of the energy bands of the adatom with respect to the Fermi level of the substrate. This view is supported by model crystal-field Hamiltonian calculations.

DOI: 10.1103/PhysRevB.93.174409

I. INTRODUCTION

Magnetic anisotropy, i.e., the preference of a system for being magnetized in a certain direction, is one of the key properties underlying the practical use of magnetic materials. One contribution to the magnetic anisotropy comes from the classical interaction of magnetic dipoles. This mechanism stands behind the so-called shape anisotropy and can be described using classical physics—although a quantum-mechanical description has been developed as well [1,2]. Another contribution, which becomes important in particular for small systems such as atomic clusters or nanostructures, comes from spin-orbit coupling (SOC). This *magnetocrystalline anisotropy* can only be described within a relativistic quantum-mechanical formalism. We will deal exclusively with this SOC-induced contribution in this work.

A quantitative measure of the magnetocrystalline anisotropy is the magnetocrystalline anisotropy energy (MAE), i.e., the difference between total energies of the system for two orientations of the magnetization $\boldsymbol{M}$. Evaluating the MAE is often numerically very difficult because one has to subtract two large numbers to get a small difference between them. To get accurate results, one has to tune several technical parameters such as an integration mesh setup in $\boldsymbol{k}$ space [3,4] or the adequacy of the basis set. For supported nanostructures, the treatment of the substrate is also very important [5,6]. A lot of attention was devoted to these issues recently.

Nevertheless, there is also another line of research on the magnetocrystalline anisotropy, namely the effort to understand its mechanism intuitively and, in particular, to see which electronic structure features participate in the phenomenon. One possibility is to use perturbation theory and to describe spin-orbit interaction approximately within the two-component formalism by the SOC term $H_{\mathrm{SOC}} = \xi \boldsymbol{L} \cdot \boldsymbol{S}$, where L and S are the orbital and spin angular momentum operators and ξ is the SOC strength. For systems studied here, the lowest-order nonvanishing contribution to the total energy is the second-order term,

$$\Delta E^{(2)} = - \sum_{\substack{i \in \mathrm{occ} \\ j \in \mathrm{unocc}}} \frac{|\langle \psi_i | H_{\mathrm{SOC}} | \psi_j \rangle|^2}{E_j - E_i}. \qquad (1)$$

Relying on second-order perturbation theory has led to concepts such as scaling of the MAE with the square of the SOC strength or the frequently used Bruno and van der Laan formulas relating the MAE to the anisotropy of the orbital magnetic moment [7–11]. On the other hand, as the sum in Eq. (1) involves a large number of summands that may be of comparable magnitude, it may be very difficult to identify just a few terms as the dominant ones and in this way to link MAE of a particular system to specific features in the electronic structure. Getting a simple intuitive understanding of the MAE by looking at the interaction between individual states thus may be very hard to achieve—despite the effort and interesting results obtained [12–14]. Approaches that focus on integral quantities such as a corresponding susceptibility (still within second-order perturbation theory) could have a more general use [11].

However, other mechanisms for generating the magnetocrystalline anisotropy, not accounted for by second-order perturbation theory, are also possible and were discussed in the past. In particular, Eq. (1) cannot be used if degenerate levels are coupled. For that situation, another mechanism contributing to the MAE was suggested, namely a SOC-induced splitting of states that would be degenerate otherwise [3,11,15–17]. If some of these states are pushed above or below the Fermi level E_F, a large change of the total energy occurs. For layered and bulk systems, this effect may not be dominant because relevant states occupy only a restricted region in $\boldsymbol{k}$ space [13,17,18]. However, the situation could be different for adatoms and clusters, where there is no dispersion in $\boldsymbol{k}$ space.

The question then remains whether there exist in reality systems where the origin of magnetocrystalline anisotropy can be traced to a SOC-induced splitting of otherwise degenerate states at E_F and where this mechanism can be effectively

*sipr@fzu.cz; http://www.fzu.cz/∼sipr

visualized in terms of integral quantities such as the density of states (DOS). Such a mechanism could give rise to a large MAE. In fact, lately there have been intensive efforts to understand how the MAE could be made as large as possible [19–23]. A better intuitive insight into the magnetocrystalline anisotropy beyond the perturbation theory might be useful in this context. From a more general point of view, it is desirable to have a framework that would enable us to visualize the emergence of the magnetocrystalline anisotropy by means of simple concepts.

We decided, therefore, to perform a detailed *ab initio*, i.e., material-specific study of magnetocrystalline anisotropy for Fe, Co, and Ni adatoms and monolayers on Au(111). The motivation for this choice is that only a little hybridization between 3*d* states and Au states is expected [24]. For adatoms, the 3*d* states could thus have an atomiclike character where the effect of SOC-induced splitting of states should be larger than for delocalized states. Comparison between adatoms and monolayers could further elucidate the role of different factors. We employ a fully relativistic framework (solving the four-component Dirac equation) to treat the SOC as accurately as possible. The application of the Green-function formalism allows a proper treatment of adatoms, avoiding possible artefacts that might arise from a supercell approach.

Our paper is organized as follows. First we introduce our computational method and the investigated systems. Then we present numerical values of MAE and magnetic moments. The main emphasis is on showing how the SOC affects the DOS resolved into components according to the magnetic quantum numbers. We demonstrate that the effect of SOC is much larger if the magnetization is perpendicular to the plane than if it is in-plane. This effect is reproduced using a simple crystal-field Hamiltonian. Some technical details related to projecting the DOS onto magnetic quantum number components for a magnetic system are described in the Appendixes.

II. METHODS

A. Computational scheme

The electronic structure is calculated within the *ab initio* spin-density-functional framework, relying on the local-spin-density approximation with the Vosko, Wilk, and Nusair parametrization for the exchange and correlation potential [25]. The electronic structure is described, including all relativistic effects, by the Dirac equation, which is solved using the spin-polarized relativistic multiple-scattering or Korringa-Kohn-Rostoker (KKR) Green-function formalism [26] as implemented in the SPRKKR code [27]. The potential was treated within the atomic-sphere approximation (ASA). For the multipole expansion of the Green function, the angular momentum cutoff $\ell_{\max} = 3$ was used. The energy integrals were evaluated by contour integration on a semicircular path within the complex energy plane using a Gaussian mesh of 32 points. The integration over the **k** points was done on a regular mesh, using 10 000 points in the full surface Brillouin zone.

This work deals with adatoms and monolayers on a substrate. The Green-function formalism allows us to treat the substrate as truly semi-infinite: the electronic structure is relaxed within the topmost seven substrate layers, while at the bottom of this relaxation zone the electronic structure is matched to the bulk via the decimation technique. Monolayers are dealt with in the same manner as the clean substrate, just adding a layer of 3*d* atoms on top. The vacuum is represented by four layers of empty spheres. Adatoms are treated as embedded impurities: first one calculates the electronic structure of a semi-infinite host and then solves the Dyson equation for an embedded impurity cluster [28]. The impurity clusters we used contain 62 sites in total; this includes one 3*d* adatom, 25 substrate atoms, and the rest are empty spheres.

The MAE is calculated as a difference of total energies for $\boldsymbol{M} \| \hat{\boldsymbol{x}}$ and $\boldsymbol{M} \| \hat{\boldsymbol{z}}$,

$$E_{\mathrm{MCA}} = E^{(x)} - E^{(z)}. \tag{2}$$

Accordingly, a positive MAE means that the easy axis of magnetization is out-of-plane.

If the Dirac equation is used, the influence of SOC cannot be isolated in a straightforward way. One can achieve it, nevertheless, using an approximate two-component scheme [29] where the SOC-related term is identified via relying on a set of approximate radial Dirac equations. This scheme was used in the past to investigate the influence of SOC on various properties including the MAE [6]. In this work, we use this scheme to suppress the SOC when investigating the DOS in Sec. III B. If SOC is to be included, the DOS can be calculated either using the full Dirac equation or using the approximative scheme [29]; the corresponding curves in the graphs agree within the thickness of the line, demonstrating that both schemes are equivalent as concerns the DOS. On the other hand, there are small yet identifiable differences between both schemes concerning the MAE (about 10% in the case of adatoms and about 20% in the case of monolayers). The results presented in Sec. III A were obtained using the fully relativistic scheme.

B. Investigated systems

We investigated Fe, Co, and Ni adatoms and monolayers on the fcc Au(111) surface. The corresponding structures are shown in Fig. 1. To get proper interatomic distances, we performed geometry optimization using the VASP code [30,31]. These calculations were done for slabs of three layers of substrate atoms covered either by a complete layer of 3*d* atoms (for monolayers) or by a 3×3 surface supercell of 3*d* atoms (for adatoms). The positions of the substrate atoms

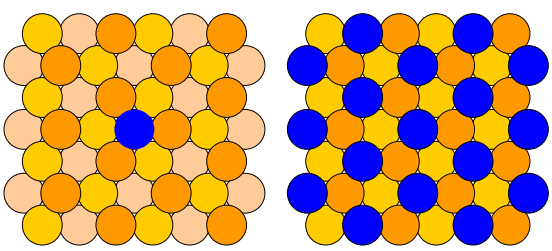

FIG. 1. Structure diagrams for an adatom and a monolayer on an Au(111) surface. The 3*d* atoms are represented by blue (dark) circles, and various shades of orange (gray) represent Au atoms in different layers.

TABLE I. Vertical distances $z_{3d\text{-Au}}$ in Å between the layer containing the 3d atoms and the nearest layer containing Au atoms.

3d	$z_{3d\text{-Au}}$ adatom	$z_{3d\text{-Au}}$ monolayer
Fe	1.889	2.088
Co	1.856	2.035
Ni	1.820	2.016

in the two lowermost layers were fixed while the positions of the topmost substrate atoms and 3d atoms were relaxed. This led to a mild buckling of the topmost Au layer for the adatoms (about 0.02 Å), which we ignored in subsequent KKR–Green-function calculations. Using a three-layer-thick slab instead of a semi-infinite substrate is justified if one is interested in relaxing the positions of the 3d atoms above the host. However, using it for evaluating the MAE would be inappropriate—for that, either a much thicker slab (as in Ref. [5]) or a proper semi-infinite crystal (as in this work) should be employed.

The optimized structural parameters as we took them from VASP calculations and used in the SPRKKR calculations are summarized in Table I. As concerns the distances between Au substrate layers, we used the bulk interatomic distance 2.396 Å everywhere except for the distance for the topmost Au layer, which we took to be 2.431 Å for adatoms and 2.427 Å for monolayers (as obtained via the VASP calculations).

III. RESULTS

A. MAE and magnetic moments

The results obtained for the MAE and magnetic moments are presented in Table II. One can see that the easy axis of the magnetization is perpendicular to the surface for Fe and Co adatoms and monolayers and parallel to the surface for Ni adatom and monolayer. The magnetic moments were evaluated within atomic spheres around the 3d atoms. Magnetic moments for Au atoms are small. In the case of adatoms, the total magnetic moment induced in the Au substrate amounts to about 5 % of the 3d adatom moment and is oriented parallel to the moment of the adatom. In the case of monolayers, the total magnetic moment induced in the Au substrate per a 3d atom is about 2% of the 3d atom moment and is oriented antiparallel to the moments of the 3d atoms.

TABLE II. Magnetic properties of 3d adatoms and monolayers on Au(111). The first two columns identify the system, the third column shows the MAE obtained as a difference of total energies (in meV per 3d atom), the fourth column shows spin magnetic moments for $\boldsymbol{M}\|\hat{\boldsymbol{z}}$, and the fifth and sixth columns show orbital magnetic moments for $\boldsymbol{M}\|\hat{\boldsymbol{z}}$ and $\boldsymbol{M}\|\hat{\boldsymbol{x}}$, respectively. Magnetic moments are in units of μ_B.

		E_{MCA}	$\mu^{(z)}_{\mathrm{spin}}$	$\mu^{(z)}_{\mathrm{orb}}$	$\mu^{(x)}_{\mathrm{orb}}$
Fe	adatom	4.07	3.40	0.536	0.062
	monolayer	0.97	3.08	0.127	0.073
Co	adatom	4.42	2.13	0.218	0.206
	monolayer	0.42	2.01	0.156	0.168
Ni	adatom	− 1.63	0.67	0.063	0.158
	monolayer	− 1.97	0.73	0.118	0.191

The spin moments μ_{spin} practically do not depend on the magnetization direction, while the orbital moments μ_{orb} strongly depend on it. For Fe and Ni atoms, μ_{orb} is significantly larger if $\boldsymbol{M}$ is parallel to the easy axis of the magnetization than if $\boldsymbol{M}$ is parallel to the hard axis—in agreement with the expectations based on second-order perturbation theory [7–9]. Surprisingly, this is not the case for Co, where for the adatom the value of μ_{orb} depends only slightly on the $\boldsymbol{M}$ direction, and for the monolayer the trend is even reversed.

B. Density of states

We first look at the spin-projected density of states in a range covering the whole valence region. This is presented in Fig. 2. The data correspond to $\boldsymbol{M}\|\hat{\boldsymbol{z}}$ but the plot would look practically the same also for $\boldsymbol{M}\|\hat{\boldsymbol{x}}$ at this scale. There is a considerable overlap between 3d majority-spin states and Au states, implying that majority-spin states are affected by hybridization while minority-spin states are more atomiclike.

One can see that the majority-spin states are nearly fully occupied. The Fermi level E_F is around the middle of the minority-spin band. Thus if we are interested in the possible effects of shifting the states across E_F, we should focus on the influence of the SOC on the minority-spin states. Restricting ourselves to the minority-spin states will greatly simplify further analysis without missing the important aspects.

Studying how the m-resolved DOS varies upon the rotation of the magnetization requires some clarifications. The projection of the DOS according to the quantum number m has to be done always in the same reference frame, disregarding the orientation of $\boldsymbol{M}$. We call this frame the "global reference frame"—it is fixed to the underlying crystal lattice. If the m projections are done in different reference frames for different magnetization directions, the definitions of the m components themselves also vary because they are linked to the spherical harmonics $Y_{\ell m}$, which are defined with respect to the x, y, and z axes. On the other hand, if one wants to retain and emphasize the difference between spin-up and spin-down contributions to the DOS, one has to make the projection in a "local reference frame," rotated so that the z axis coincides with the magnetization direction. The need for this can be easily seen from the Stern-Gerlach term in the Pauli equation, $\boldsymbol{\sigma}\cdot\boldsymbol{B}$, which is diagonal only if the effective magnetic field $\boldsymbol{B}$ is parallel to the z axis. If the spin quantization axis is not parallel to the magnetization direction, the chosen representation strongly mixes spin-up and spin-down components.

These two circumstances suggest that if one wants to study the DOS for different directions of the magnetization $\boldsymbol{M}$, one has to renounce either having a universal definition of the m projections or retaining well-separated spin-resolved DOS components. This is not an issue if the SOC is ignored because then the direction of the magnetization has no effect on the electronic structure anyway. However, if the SOC is accounted for and the dependence of the DOS on the direction of $\boldsymbol{M}$ is in focus, this is a serious obstacle.

Fortunately, this restriction can be bypassed in our case. It is possible to get well-defined spin-minority DOS m-decomposed in a global reference frame even if $\boldsymbol{M}$ is is not

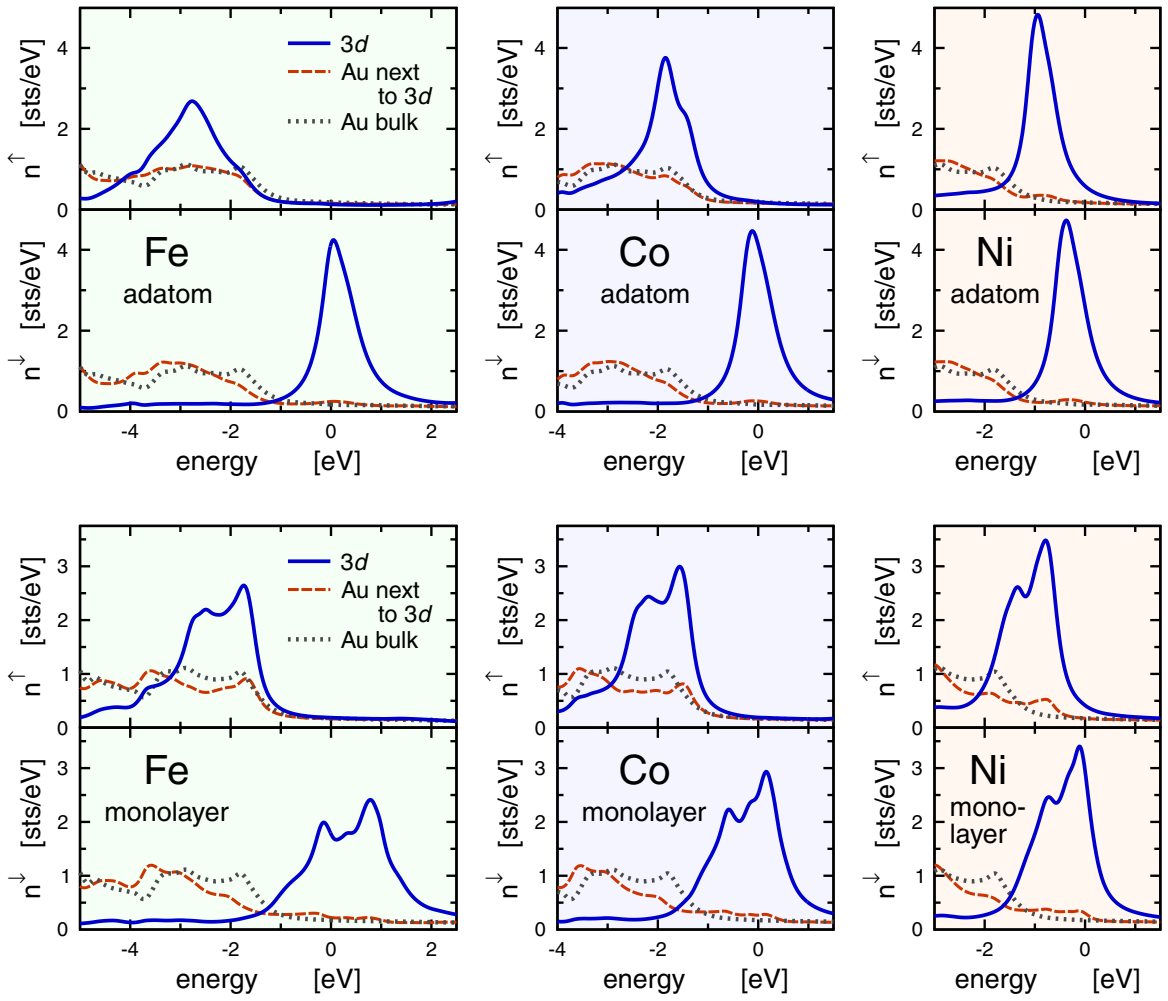

FIG. 2. Spin-projected DOS for 3*d* adatoms and monolayers on Au(111) (in states per eV) for $\boldsymbol{M}\|\hat{\boldsymbol{z}}$. Full lines represent the DOS related to 3*d* atoms, dashed lines represent the DOS related to those Au atoms that are nearest neighbors to 3*d* atoms, and dotted lines represent the DOS for bulk Au.

parallel to the z axis, relying on an approximate procedure that is described in Appendix A. The procedure combines results for an m decomposition in global and local reference frames. Employing this technique, we obtained the density of minority-spin d states resolved according to the magnetic quantum number m as shown in Figs. 3–5. The magnetization is either out-of-plane ($\boldsymbol{M}\|\hat{\boldsymbol{z}}$, $\theta = 0°$) or in-plane ($\boldsymbol{M}\|\hat{\boldsymbol{x}}$, $\theta = 90°$), and the m projections are defined in the same (global) reference frame in both cases. To highlight the effect of the SOC, we present results obtained with SOC suppressed and with SOC accounted for.

It can be seen readily from the plots in Figs. 3–5 that if the SOC is suppressed, the DOS does not depend on the sign of m. Components for $+|m|$ and $-|m|$ are the same in this case; the only splitting comes from the crystal field. If the SOC is taken into account, then the DOS depends further on whether m is positive or negative. There is a significant difference in how the $\pm|m|$ states are split for out-of-plane magnetization and for in-plane magnetization (especially for the $m = \pm 2$ case).

The procedure outlined in Appendix A can be applied only if the SOC-induced splitting of the majority-spin states is negligible in the energy region in which we are interested, i.e., around E_F. This assumption is well justified for Fe and Co. However, it is not so good for Ni, where the exchange splitting is quite small (cf. Fig. 2) and the influence of the SOC on the majority-spin DOS is significant up to about 0.5 eV below E_F. Therefore, for Ni we present the data only for $E > -0.6$ eV and even there they are less reliable than analogous data in Figs. 3 and 4. The full energy range for $\boldsymbol{M}\|\hat{\boldsymbol{x}}$ is covered by Figs. 9–11 in Appendix B, where we present the m-resolved DOS projected in a local reference frame rotated so that the $z^{(\mathrm{loc})}$ axis is parallel to $\boldsymbol{M}$. (For $\boldsymbol{M}\|\hat{\boldsymbol{z}}$, the global reference frame and the local reference frame coincide, because $z^{(\mathrm{loc})}$ is then identical with z.)

The definitions of individual m-components employed in Appendix B and employed in this section obviously differ. One cannot, therefore, directly compare the plots where the DOS was resolved into m-components in the global reference frame (Figs. 3–5) with plots where the DOS was resolved in the local reference frame (Appendix B). What is common in both reference frames is that the SOC-induced splitting of the $\pm|m|$ components it significantly smaller for $\boldsymbol{M}\|\hat{\boldsymbol{x}}$ than for $\boldsymbol{M}\|\hat{\boldsymbol{z}}$.

Let us summarize the picture obtained by inspecting the DOS. First, note that the minority-spin DOS for the adatoms has quite an atomic character: if the SOC is suppressed, it can be seen as representing just three broadened atomic levels,

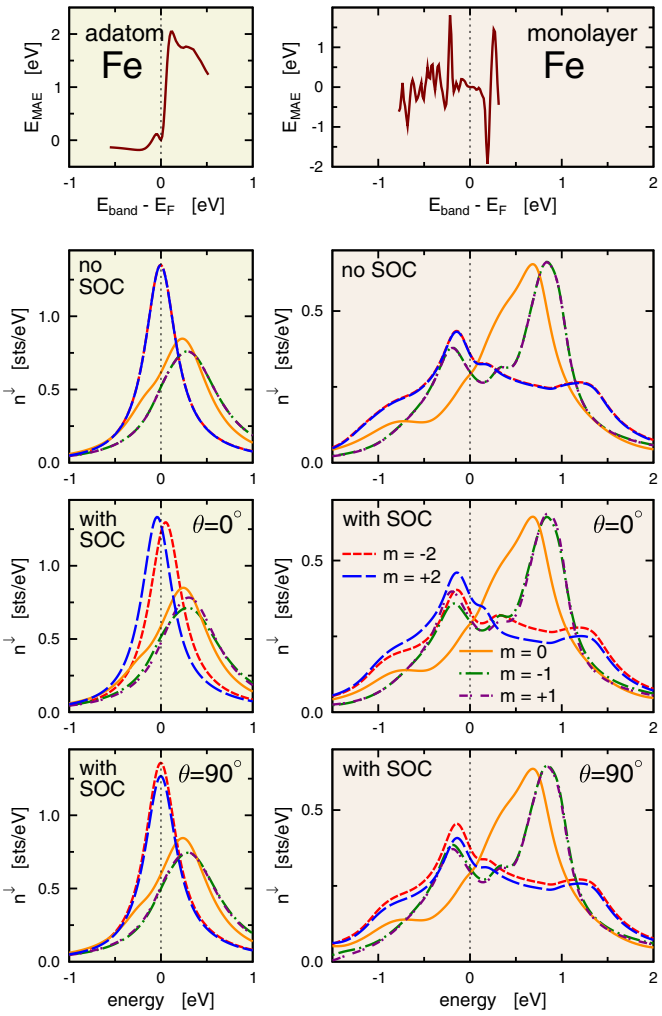

FIG. 3. The d component of the minority-spin DOS for a Fe adatom (left) and a Fe monolayer (right) on Au(111), resolved according to the magnetic quantum number m. The case when the SOC is suppressed is presented together with the case when the SOC is included. The magnetization is either perpendicular to the surface ($\theta = 0^\circ$) or parallel to the surface ($\theta = 90^\circ$). The dependence of the MAE on the position of the top of the valence band is shown in the top graphs.

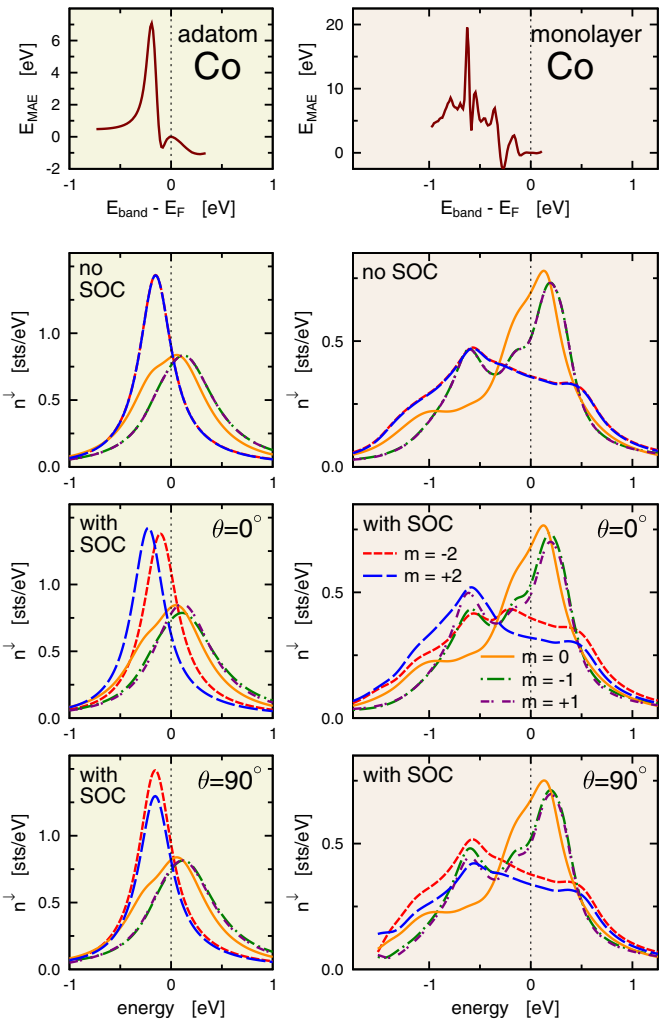

FIG. 4. Density of the minority-spin d states resolved according to the magnetic quantum number m and the dependence of the MAE on the position of the top of the valence band for a Co adatom (left graphs) and a Co monolayer (right graphs) on Au(111). Otherwise, this figure is analogous to Fig. 3.

depending on $|m|$. For monolayers, the hybridization between states from different $3d$ atoms is considerable, so the DOS does not have an atomic character anymore. The second point to emphasize is that the influence of the SOC is significantly larger for $\theta = 0^\circ$ than for $\theta = 90^\circ$. More specifically, for $\theta = 0^\circ$ the SOC splits the $m = \pm 2$ peak into two and shifts their positions in different directions, while for $\theta = 90^\circ$ the peak positions remain the same (only their intensities change).

The splitting of m-resolved DOS peaks by the SOC suggests that the MAE could be very sensitive to the position of E_F with respect to these peaks. Therefore, we calculated the MAE while varying the position of the top of the valence band E_{band}, i.e., the band filling. The results are shown in the top panels of Figs. 3–5. One can see that for the adatoms there is indeed a sharp peak in the MAE just at the energy where there is a peak for the $|m| = 2$ component in the case of no SOC. This is especially visible for Co and Ni adatoms. For the Fe adatom, this aspect is overshadowed by another strong feature stemming from the fact that, in this case, also the $|m| = 1$ states are affected by SOC. The situation for monolayers is more complicated because the m-components are not atomiclike anymore. Nevertheless, even here a strong peak in the curve for E_{MAE} as a function of E_{band} appears at the energy where the DOS components for $|m| = 2$ have their maximum. We would like to note in this context that the density of the E_{band} mesh used in the calculation is the same for adatoms and monolayers. This means that the observation that the $E_{\text{MAE}}(E_{\text{band}})$ oscillations are much wilder for monolayers than for adatoms describes a real effect. This is probably due to hybridization between $3d$ atoms, which is present for monolayers but absent for adatoms.

C. Effect of SOC on the energy levels via model Hamiltonian

We could see in Sec. III B how the SOC splits electronic states for different orientations of the magnetization. Let us check to what extent this can be described within a simple

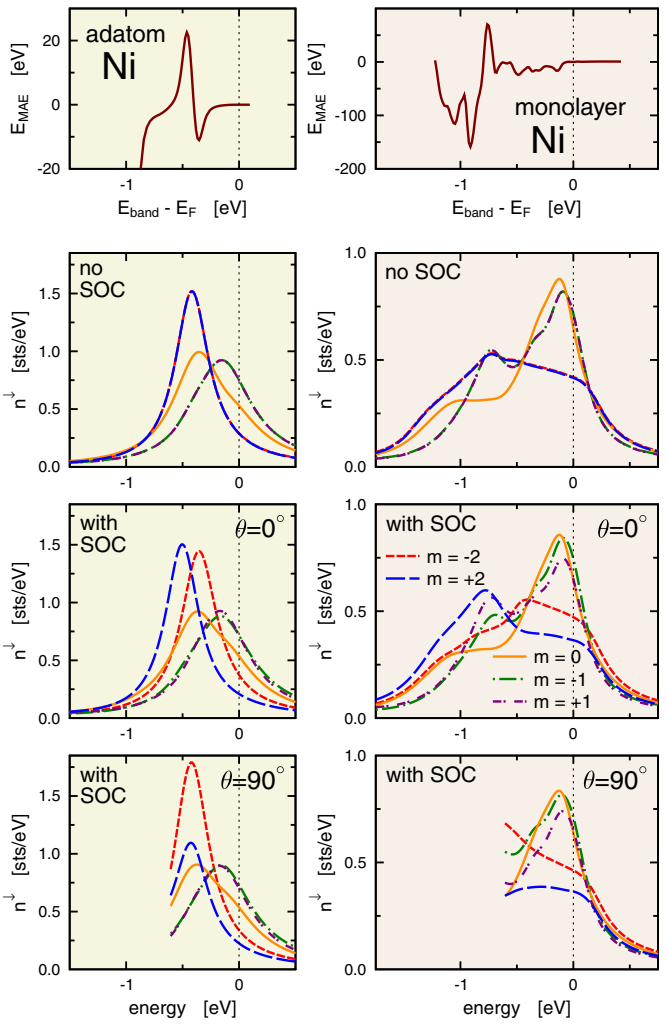

FIG. 5. Density of the minority-spin d states resolved according to the magnetic quantum number m and the dependence of the MAE on the position of the top of the valence band for a Ni adatom (left graphs) and a Ni monolayer (right graphs) on Au(111). Otherwise, this figure is analogous to Fig. 3.

model with only the crystal-field effects taken into account. This corresponds to a situation in which the electron feels only the Coulombic field generated by charges located at the positions of the nuclei.

To highlight the essential features, we restrict ourselves to d electrons in an axial field (corresponding to D_{4d}, i.e., antiprism symmetry). If there is no magnetic order or SOC, the crystal-field Hamiltonian is given as described, for example, in the book of Bersuker [32] [Eqs. (4.9) and (4.10) and Table 4.1]. The Hamiltonian is determined by two parameters (if the constant energy shift is omitted), resulting in three spin-degenerate energy levels as given in Table III. The order of levels E_1, E_2, and E_3 depends on the values of parameters P and Q. Levels E_1 and E_3 are doubly degenerate. Nonzero terms of the crystal-field Hamiltonian are

$$H^{(\mathrm{cry})}_{ms,m's'} = \begin{cases} P, & m = \pm 2, \quad s = s', \\ Q, & m = \pm 1, \quad s = s', \\ -2P - 2Q, & m = 0, \quad s = s'. \end{cases} \tag{3}$$

TABLE III. Energy levels of d electrons for an axial-crystal-field Hamiltonian if there is no exchange splitting and no SOC.

Energy	$Y_{\ell m}$
$E_1 = P$	$m = \pm 2$
$E_2 = -2(P + Q)$	$m = 0$
$E_3 = Q$	$m = \pm 1$

The subscript ms combines the magnetic quantum number m and the spin quantum number s, meaning that our Hamiltonian is represented by a 10×10 matrix.

The magnetization of the system is reflected by the exchange field Hamiltonian $H^{(\mathrm{ex})}$. To distinguish between two orientations of the magnetization, we keep the spin quantization axis fixed (parallel to z) and vary the Hamiltonian $H^{(\mathrm{ex})}$. The nonzero terms of $H^{(\mathrm{ex})}$ for $\boldsymbol{M} \| \hat{\boldsymbol{x}}$ are

$$H^{(\mathrm{ex})}_{ms,m's'} = B, \quad m = m', \quad s \neq s' \tag{4}$$

and for $\boldsymbol{M} \| \hat{\boldsymbol{z}}$ they are

$$H^{(\mathrm{ex})}_{ms,m's'} = B, \quad m = m', \quad s = s' = -1/2, \tag{5a}$$

$$H^{(\mathrm{ex})}_{ms,m's'} = -B, \quad m = m', \quad s = s' = +1/2. \tag{5b}$$

The third contribution to the model Hamiltonian comes from the SOC. The spin quantization axis is kept parallel to z, so the Hamiltonian $H^{(\mathrm{SOC})} = \xi \boldsymbol{L} \cdot \boldsymbol{S}$ can be represented as (cf. Stöhr [33])

$$H^{(\mathrm{SOC})} = \begin{bmatrix} -\xi & 0 & 0 & 0 & 0 & 0 & \xi & 0 & 0 & 0 \\ 0 & -\frac{\xi}{2} & 0 & 0 & 0 & 0 & 0 & \frac{\xi\sqrt{6}}{2} & 0 & 0 \\ 0 & 0 & 0 & 0 & 0 & 0 & 0 & 0 & \frac{\xi\sqrt{6}}{2} & 0 \\ 0 & 0 & 0 & \frac{\xi}{2} & 0 & 0 & 0 & 0 & 0 & \xi \\ 0 & 0 & 0 & 0 & \xi & 0 & 0 & 0 & 0 & 0 \\ 0 & 0 & 0 & 0 & 0 & \xi & 0 & 0 & 0 & 0 \\ \xi & 0 & 0 & 0 & 0 & 0 & \frac{\xi}{2} & 0 & 0 & 0 \\ 0 & \frac{\xi\sqrt{6}}{2} & 0 & 0 & 0 & 0 & 0 & 0 & 0 & 0 \\ 0 & 0 & \frac{\xi\sqrt{6}}{2} & 0 & 0 & 0 & 0 & 0 & -\frac{\xi}{2} & 0 \\ 0 & 0 & 0 & \xi & 0 & 0 & 0 & 0 & 0 & -\xi \end{bmatrix}. \tag{6}$$

The total Hamiltonian we have to diagonalize is

$$H = H^{(\mathrm{cry})} + H^{(\mathrm{ex})} + H^{(\mathrm{SOC})}. \tag{7}$$

We want to apply this model for an adatom, where the hybridization is small and the crystal-field effects will be important. Looking at the adatom-related panels of Figs. 3–5, we can see that in the absence of SOC, the minority-spin DOS indeed resembles three atomiclike energy levels, as in Table III. It is convenient to introduce level spacings

$$\Delta_1 \equiv E_2 - E_1, \tag{8}$$

$$\Delta_2 \equiv E_3 - E_2, \tag{9}$$

TABLE IV. Parameters (in eV) for the model Hamiltonian simulating 3*d* adatoms on Au(111) by means of an axial crystal field model.

	Fe	Co	Ni
Δ_1	0.24	0.21	0.06
Δ_2	0.05	0.06	0.20
$E_\downarrow - E_\uparrow$	2.81	1.96	0.57
ξ	0.065	0.085	0.108

through which we can express the model Hamiltonian parameters as

$$P = -\frac{3\Delta_1 + 2\Delta_2}{5}, \tag{10}$$

$$Q = \frac{2\Delta_1 + 3\Delta_2}{5}. \tag{11}$$

To simulate 3*d* adatoms on Au(111), one should read the Δ_1, Δ_2 splittings from Figs. 3–5 to get the values for the parameters P, Q and the exchange splitting from Fig. 2 to get the parameter B using $E_\downarrow - E_\uparrow = 2B$. The SOC parameters ξ can be obtained via *ab initio* calculations [34]. The appropriate values are given in Table IV.

A general idea of how the SOC affects the energy levels can be obtained by diagonalizing the Hamiltonian (7) for different orientations of $\boldsymbol{M}$ while the SOC strength ξ is gradually increased from zero to a realistic value. The corresponding results are presented in Fig. 6, where we show energy levels $E^\uparrow(\xi)$ and $E^\downarrow(\xi)$ for parameters given in Table IV. The "proper" value of ξ for each element is marked by a thin dashed line. To avoid confusion, we should note that our categorizing of levels as $E^\uparrow$ or $E^\downarrow$ is done just for convenience, by comparing their positions to the spin-projected DOS shown in Fig. 2. We care only about the energy levels in this context and not about the wave functions, so the issue of mixed spin character for $\theta = 90^\circ$, discussed in Sec. III B and in Appendix A, does not interfere with our analysis.

A prominent feature of Fig. 6 is that the effect of ξ is much less for in-plane magnetization ($\theta = 90^\circ$) than for perpendicular magnetization ($\theta = 0^\circ$). This is especially true for the lowest energy, which corresponds to $m = \pm 2$. By comparing this observation to Figs. 3–5, we see that the simple crystal-field model indeed accounts for the trends in the m-resolved DOS for the 3*d* adatoms. It is worth noting that if the exchange-field parameter B decreases (i.e., going from Fe to Co to Ni), the $m = \pm 2$ energy levels split also for the $\theta = 90^\circ$ case (in-plane magnetization). A similar trend can also be seen in the DOS in Sec. III B: the difference between $m = \pm 2$ curves in the lowermost left panels in Figs. 3–5 increases when going from Fe to Co to Ni.

IV. DISCUSSION

Our aim was to investigate whether markers of MAE can be seen in intuitive quantities such as the m-resolved DOS. Figures 3–5 (in conjunction with Figs. 9–11) show how SOC affects the DOS depending on the orientation of the magnetization $\boldsymbol{M}$. The corresponding changes in the DOS can be linked to the magnetocrystalline anisotropy of adatoms. Particularly for the Fe and Co adatoms, one can see that for $\theta = 0^\circ$ the SOC splits the $|m| = 2$ component of the DOS in such a way that one of the peaks is pushed above E_F (or at least an essential part of it). The band-energy contribution to the total energy is thus substantially reduced. As this effect does not occur for $\theta = 90^\circ$, the out-of-plane orientation of $\boldsymbol{M}$ is energetically more favored and the corresponding MAE is positive, in agreement with Table II.

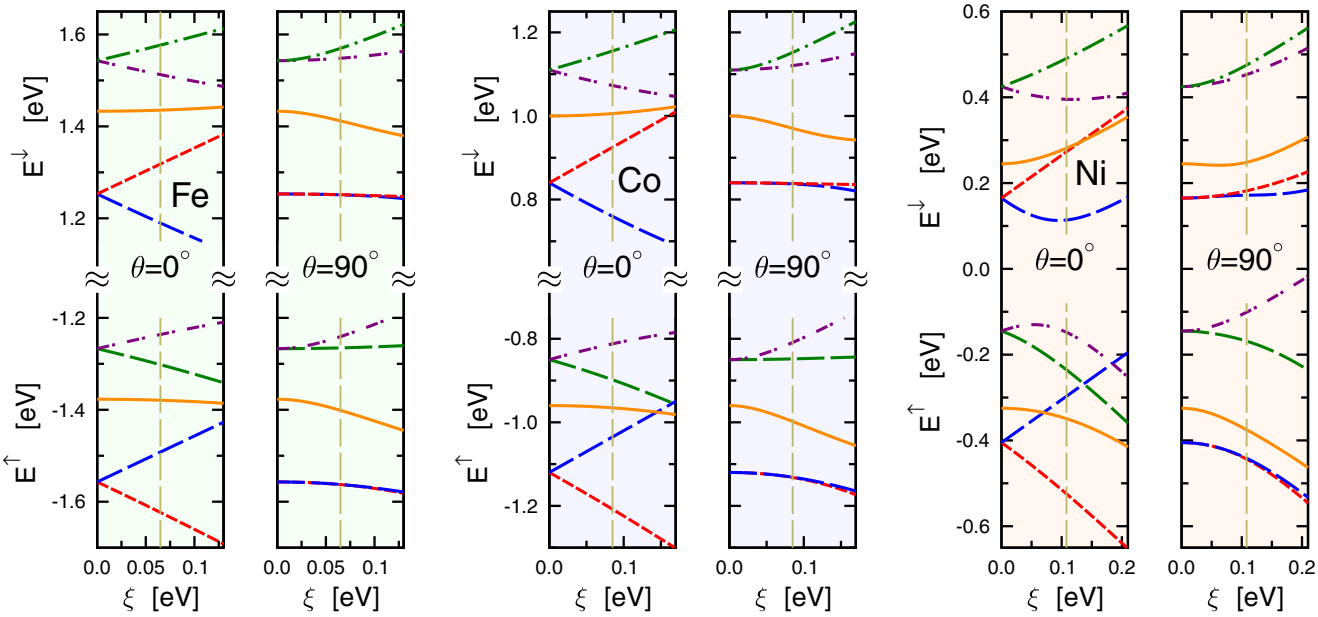

FIG. 6. Dependence of eigenenergies of the model Hamiltonian given by Eq. (7) on the SOC strength ξ for two orientations of $\boldsymbol{M}$. The model parameters for Fe, Co, and Ni adatoms are given in Table IV. Thin dashed lines mark ξ values appropriate for each element. The zero of energy corresponds to the case with no magnetization and no crystal field.

The SOC-induced splitting of the $|m| = 2$ peak occurs for $\theta = 0^\circ$ also for the Ni adatom. However, in that case both peaks remain below E_F and the change in the band energy is therefore much smaller. The influence of SOC for the $\theta = 90^\circ$ case is best seen if the m projection is done in a rotated local reference frame, as in Fig. 11. This is because the isolation of the minority-spin DOS in the global reference frame cannot be done properly due to the small energy separation between the majority-spin and minority-spin states of Ni. The lowermost graphs in Fig. 5 have to be seen as primarily illustrative in this respect because they are affected by the fact that majority-spin states are still influenced by the SOC in this region. Focusing on the unambiguous data in Fig. 11, one can see that for $\theta = 90^\circ$ the states with $|m^{(\mathrm{loc})}| = 2$ are split in such a way that part of one of the SOC-split peaks is pushed above E_F. This effect overruns the corresponding effect on the $|m| = 2$ states for $\theta = 0^\circ$ (Fig. 5), and, accordingly, the easy axis of magnetization is in-plane for the Ni adatom.

Effects of this kind can hardly be identified for monolayers. In this case, the hybridization between the $3d$ states distorts the atomiclike character of the states, and one would have to consider a lot of contributions, similarly as if the $E(\boldsymbol{k})$ band structure of layered systems is analyzed [12,14,16].

The simple crystal-field model accounts qualitatively for many aspects of the magnetocrystalline anisotropy of adatoms, indicating that this anisotropy can be understood intuitively as an interplay between the axial crystal field, the exchange field, and the spin-orbit coupling. However, there are also differences between the pictures offered by the model Hamiltonian and by the DOS obtained from *ab initio* calculations. For example, the model Hamiltonian suggests that for an in-plane magnetization ($\theta = 90^\circ$), the splitting between the $m = \pm 1$ levels is larger than the splitting between the $m = \pm 2$ levels (Fig. 6); however, we do not observe this feature in Figs. 3–5. This means that effects not included in the simple model of Sec. III C, such as hybridization, are important as well.

It should be noted that by monitoring SOC-induced changes in the DOS, one accounts only for the band-energy contribution to the total energy, omitting thus the terms that explicitly depend on the change of the potential upon rotation of $\boldsymbol{M}$ (see, e.g., Chap. 6 of the monograph of Weinberger [35] for more details). This is equivalent to relying on the so called force theorem. If the MAE is evaluated accounting for the band energy contribution only (by means of the torque method [36,37]), we obtain $E_{\mathrm{MCA}} = 5.7$ meV for the Fe adatom, 1.9 meV for the Co adatom, and -0.8 meV for the Ni adatom. Comparison with Table II that gives E_{MCA} as a difference of total energies shows that the change in the band energy does not fully account for the magnetocrystalline anisotropy but nevertheless constitutes a significant part of it. One should also keep in mind that the SOC-induced splitting of the DOS is not the only way the band energy is changed upon rotation of $\boldsymbol{M}$. For example, all effects contained in Eq. (1) contribute as well. Accordingly, what has been done here is identifying and visualizing one important mechanism contributing to the magnetocrystalline anisotropy. We suggest (following earlier hints [3,11,15–17]) that this mechanism may be the dominant one for some adatoms and small clusters on surfaces—including those that attracted a lot of attention recently [21,23,38,39].

Another interesting system to be mentioned in this context is lithium nitridoferrate $Li_2[(Li_{1-x}Fe_x)N]$, which attracted a lot of attention due to its very high magnetocrystalline anisotropy [11,40–42]. This system can be viewed as a collection of semi-isolated Fe impurities. A similar effect to the one investigated here could therefore be important for $Li_2[(Li_{1-x}Fe_x)N]$, and attention was indeed paid to it in this respect [11,42]. Generally, the mechanism we explored here should be important whenever the width of the electronic bands becomes comparable to the SOC-induced changes in the orbital-resolved DOS upon the rotation of the magnetization.

If the magnetocrystalline anisotropy is generated via pushing some SOC-split levels across the Fermi level, it must crucially depend on their mutual positions. Specifically in our case, it must depend on the position of the energy bands of the adatom with respect to the Fermi level of the substrate (cf. also the top graphs of Figs. 3–5). Therefore, one might be able to manipulate the MAE by changing the substrate E_F, e.g., via doping.

Even though the aim of this study is not to reproduce experimental MAE for specific systems, it is useful to compare our values of MAE with available experiments. There are no data for adatoms on Au(111), but there have been several experimental studies of Fe and Co layers on Au(111). Before comparison with experiment is done, the dipole or shape anisotropy energy for monolayers must be given. It is -0.18, -0.08, and -0.01 meV for Fe, Co, and Ni monolayers, respectively. These values are smaller than the magnetocrystalline anisotropy energy given in Table II. So we predict that Fe and Co monolayers on Au(111) have out-of-plane easy axes of magnetization, and a Ni monolayer (for which there are no experiments available) has an in-plane easy axis of magnetization. Earlier calculations for a Co monolayer on Au(111) predicted an in-plane easy axis of magnetization for this system [6,43]; the reason for the difference is almost certainly the structural relaxation, which was accounted for here but not in the two earlier works.

Despite several experimental studies of magnetocrystalline anisotropy of Fe and Co layers on Au(111) done in the past, drawing conclusions from them is not easy or unambiguous because the growth conditions vary and typically do not favor formation of a single monolayer. A critical analysis of experiments is beyond our scope. For a Fe monolayer, it is probably safe to say that experiment suggests an out-of-plane easy axis [44–47], as our calculations do. For a Co monolayer, the situation is more complicated. For bilayer islands on Au(111), one gets an out-of-plane easy axis [48–50]. Again growth conditions may be crucial [51]. No data seem to exist for a single monolayer on Au(111). As a whole, even though we cannot verify our results by a comprehensive comparison with experiment, agreement with available data as well as the fact that our values of MAE are in the same range of values as those obtained for similar systems indicate that our results are reliable and can be used as a basis for the analysis we performed in Secs. III B and III C.

V. CONCLUSIONS

The effect of spin-orbit coupling on adatoms that only weakly hybridize with a substrate consists in splitting atom-

iclike levels that would be degenerate in its absence. The splitting is much larger if the magnetization is oriented perpendicular to the surface than if it is oriented parallel to the surface, and it can be viewed as a combined result of crystal field, exchange splitting, and spin-orbit coupling. If the originally degenerate level is close to the Fermi level, one of the peaks can be pushed above it, thereby decreasing the energy of the system. This effect represents a significant contribution to the magnetocrystalline anisotropy of adatoms. If hybridization smears out the atomiclike character of energy levels, as is the case for monolayers, this effect is not so important.

ACKNOWLEDGMENTS

This work was supported by the Grant Agency of the Czech Republic within the project 108/11/0853, by the Deutsche Forschungsgemeinschaft within the project SFB 689 "Spinphänomene in reduzierten Dimensionen," and by Ministry of Education, Youth and Sports (Czech Republic) within the project CENTEM PLUS (LO1402).

APPENDIX A: SPIN-RESOLVED AND m-RESOLVED DOS FOR $\boldsymbol{M} \nparallel \hat{z}$

It was argued in Sec. III B that if one wants to see how individual m components of the DOS are affected by the rotation of the magnetization $\boldsymbol{M}$, one should perform the m projections always in a global reference frame so that the definitions of the m components remain the same. However, when $\boldsymbol{M} \nparallel \hat{z}$, projecting the DOS in a global reference frame mixes the spin components because the spin quantization axis is no longer parallel to $\boldsymbol{M}$. In this appendix, we present a method to restore the separation of spin components in the DOS even in such a case. Our goal is achieved by a detour, combining results of projections in the global and local reference frames. Effectively, it could be seen as a way to make the spin projection and the m projection in different reference frames.

Let us recall that inside an atomic sphere, the DOS for a spin channel can be represented by means of the Green function $G(E)$ as

$$n(E) = -\frac{1}{\pi}\mathrm{Im}\int d^3\boldsymbol{r}\langle \boldsymbol{r}|G(E)|\boldsymbol{r}\rangle. \tag{A1}$$

We omit the spin labels here for brevity. Angular-momentum projections of $n(E)$ can be obtained by means of spherical harmonics. These spherical harmonics $Y_{\ell m}$ can be defined in a global reference frame (fixed to the crystal lattice) or in a local reference frame chosen so that the $z^{(\mathrm{loc})}$ axis is parallel to $\boldsymbol{M}$. The way the DOS components n_L are defined thus depends on the reference frame. We can write schematically (again, for each spin channel)

$$n_L^{(\mathrm{glo})}(E) = -\frac{1}{\pi}\mathrm{Im}\langle Y_L^{(\mathrm{glo})}|G(E)|Y_L^{(\mathrm{glo})}\rangle, \tag{A2}$$

$$n_L^{(\mathrm{loc})}(E) = -\frac{1}{\pi}\mathrm{Im}\langle Y_L^{(\mathrm{loc})}|G(E)|Y_L^{(\mathrm{loc})}\rangle. \tag{A3}$$

Integration over the radial coordinate is implicitly assumed.

We start by projecting the DOS in the local reference frame, where $\boldsymbol{M}\|\hat{\boldsymbol{z}}^{(\mathrm{loc})}$. In this way, we perform the separation of the spin components. We assume that this separation was performed "once for all times," i.e., it will be preserved during the whole subsequent procedure. All the manipulations will be applied to minority-spin DOS and to majority-spin DOS separately.

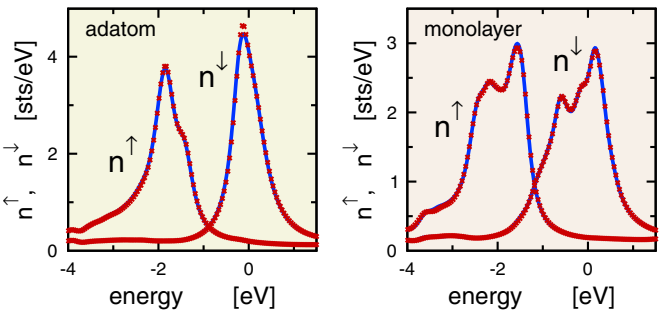

FIG. 7. Spin-projected DOS for a Co adatom and a Co monolayers on Au(111) for $\boldsymbol{M}\|\hat{\boldsymbol{z}}$ (solid blue lines) and for $\boldsymbol{M}\|\hat{\boldsymbol{x}}$ (red cross markers).

This requires a further comment. By doing the spin projection in the rotated local reference frame, we get spin-up and spin-down states assuming that the spin quantization axis is in a general direction, while when dealing with the global reference frame, the spin-quantization axis is fixed and parallel to z. However, this difference can be neglected in our case: we checked that the spin-projected DOS (without any m decomposition) looks practically the same regardless of whether the magnetization is in-plane or out-of-plane. As an illustration, the spin-projected DOS for a Co adatom and a Co monolayer is shown in Fig. 7 for two magnetization directions. These spin projections were obtained in local reference frames defined so that the $z^{(\mathrm{loc})}$ axis is always parallel to $\boldsymbol{M}$. One can see that there is hardly any difference between the DOS for $\boldsymbol{M}\|\hat{\boldsymbol{x}}$ and $\boldsymbol{M}\|\hat{\boldsymbol{z}}$. Another hint that the spin projections can be maintained upon rotating $\boldsymbol{M}$ comes from the fact that if the magnetization is rotated, the spin magnetic moments almost do not change. There is a common experience that this is the case for all magnetic systems. By assuming that the spin-projected DOS does not depend on the direction of the magnetization, we make an effective decoupling of spin and orbital degrees of freedom. This enables us to focus on changes in the m-resolved components. A similar decoupling is used, e.g., when deriving useful relations for the angular dependence of the magnetic dipole term T_z for analyzing the x-ray magnetic circular dichroism spectra [52,53].

So far we have obtained minority-spin DOS and majority-spin DOS, m-resolved in the local frame. Now we need to transform the spin-polarized DOS from the basis spanned by $Y_L^{(\mathrm{loc})}$ to the basis spanned by $Y_L^{(\mathrm{glo})}$. A straightforward transformation between the $n_L^{(\mathrm{loc})}$ and the $n_L^{(\mathrm{glo})}$ components is generally not possible—one always has to start with the Green function G to get n_L in a new basis. However, the transformation can be done provided that G is diagonal in the basis in which n_L has been initially known. Indeed, if we assume that

$$\langle Y_L^{(\mathrm{glo})}|G(E)|Y_{L'}^{(\mathrm{glo})}\rangle = \delta_{LL'}\langle Y_L^{(\mathrm{glo})}|G(E)|Y_L^{(\mathrm{glo})}\rangle,$$

we obtain

$$\begin{aligned} n_L^{(\mathrm{loc})}(E) &= -\frac{1}{\pi}\mathrm{Im}\langle Y_L^{(\mathrm{loc})}|G(E)|Y_L^{(\mathrm{loc})}\rangle, \\ &= -\frac{1}{\pi}\mathrm{Im}\sum_{L'L''}\langle Y_L^{(\mathrm{loc})}|Y_{L'}^{(\mathrm{glo})}\rangle\langle Y_{L'}^{(\mathrm{glo})}|G(E)|Y_{L''}^{(\mathrm{glo})}\rangle \\ &\quad\times\langle Y_{L''}^{(\mathrm{glo})}|Y_L^{(\mathrm{loc})}\rangle, \\ &= \sum_{L'}|\langle Y_L^{(\mathrm{loc})}|Y_{L'}^{(\mathrm{glo})}\rangle|^2\left(-\frac{1}{\pi}\right)\mathrm{Im}\langle Y_{L'}^{(\mathrm{glo})}|G(E)|Y_{L'}^{(\mathrm{glo})}\rangle, \\ &= \sum_{L'}U_{LL'}\,n_{L'}^{(\mathrm{glo})}(E). \end{aligned} \tag{A4}$$

Specifically in our case, we need to describe the situation for in-plane magnetization, i.e., $\boldsymbol{M}\|\hat{\boldsymbol{x}}$. The local reference frame is then defined by the rotation $y\to y^{(\mathrm{loc})}$, $z\to x^{(\mathrm{loc})}$, $x\to -z^{(\mathrm{loc})}$. Considering the explicit forms of $Y_{\ell m}^{(\mathrm{glo})}$ and $Y_{\ell m}^{(\mathrm{loc})}$ for $\ell=\ell'=2$, one gets for the d states

$$U_{mm'}\equiv|\langle Y_{2m}^{(\mathrm{loc})}|Y_{2m'}^{(\mathrm{glo})}\rangle|^2=\begin{bmatrix} \frac{1}{16} & \frac{1}{4} & \frac{3}{8} & \frac{1}{4} & \frac{1}{16} \\ \frac{1}{4} & \frac{1}{4} & 0 & \frac{1}{4} & \frac{1}{4} \\ \frac{3}{8} & 0 & \frac{1}{4} & 0 & \frac{3}{8} \\ \frac{1}{4} & \frac{1}{4} & 0 & \frac{1}{4} & \frac{1}{4} \\ \frac{1}{16} & \frac{1}{4} & \frac{3}{8} & \frac{1}{4} & \frac{1}{16} \end{bmatrix}. \tag{A5}$$

More generally, the transformation between the bases is given by Wigner matrices [54].

Strictly speaking, Eq. (A4) with matrix U defined in (A5) can be used only if the Green function G is diagonal in the L indices. This is generally not the case (depending on the symmetry of the system). Fortunately, nondiagonal elements of $\langle Y_L^{(\mathrm{glo})}|G|Y_{L'}^{(\mathrm{glo})}\rangle$ are small and can be neglected for the systems with which we are dealing. We verified this explicitly: If $n_L^{(\mathrm{loc})}$ is obtained from $n_L^{(\mathrm{glo})}$ by the transformation (A4), the m-resolved DOS curves obtained thereby agree within the thickness of the line with curves obtained directly from the Green function via Eq. (A3). It should be noted that this verification ought to be applied to a sum of the spin components, because for $\boldsymbol{M}\nparallel\hat{\boldsymbol{z}}$ the spin components in $n_L^{(\mathrm{glo})}$ are mixed if they are evaluated directly. Additionally, the SOC has to be suppressed to get exact equalities.

So far we found a transformation from the global frame to the local frame. However, we started our procedure by finding spin-projected DOS in the local reference frame, so we need an opposite transformation, from the local frame to the global frame. A procedure analogous to that we used to derive Eqs. (A4) and (A5) cannot be used, because if the Green function is evaluated in the rotated local reference frame, its nondiagonal elements $\langle Y_L^{(\mathrm{loc})}|G|Y_{L'}^{(\mathrm{loc})}\rangle$ cannot be neglected (the $z^{(\mathrm{loc})}$ axis of the rotated frame is chosen in an "inconvenient" way—parallel to the surface). That means we have only Eq. (A4) at our disposal and the transformation from $n_L^{(\mathrm{loc})}$ to $n_L^{(\mathrm{glo})}$ has to be accomplished by inverting it.

The inversion of the transformation matrix U defined by Eq. (A5) cannot be done straightforwardly because this matrix is singular. However, the singular 5×5 matrix U of Eq. (A5) can be folded down to a regular 3×3 matrix $U^{(\mathrm{fold})}$ if we assume that the m components do not depend on the sign of m, i.e., if

$$n_{|m|}^{(\mathrm{glo})}=n_{-|m|}^{(\mathrm{glo})}. \tag{A6}$$

In such a case, one does not have to deal with all five independent components $n_{-2}^{(\mathrm{glo})},\ldots,n_2^{(\mathrm{glo})}$. It is enough to keep three of them, $n_{-2}^{(\mathrm{glo})}$, $n_{-1}^{(\mathrm{glo})}$, $n_0^{(\mathrm{glo})}$, and the remaining two can be recovered by taking $n_2^{(\mathrm{glo})}=n_{-2}^{(\mathrm{glo})}$ and $n_1^{(\mathrm{glo})}=n_{-1}^{(\mathrm{glo})}$. This means that the original Eq. (A4), which we write here in a more explicit form as

$$n_m^{(\mathrm{loc})}(E)=\sum_{m'=-2}^{2}U_{mm'}n_{m'}^{(\mathrm{glo})}(E),\quad m=-2,\ldots,2,$$

is reduced to

$$n_m^{(\mathrm{loc})}(E)=\sum_{m'=-2}^{0}U_{mm'}^{(\mathrm{fold})}n_{m'}^{(\mathrm{glo})}(E),\quad m=-2,-1,0 \tag{A7}$$

with

$$U_{mm'}^{(\mathrm{fold})}=\begin{bmatrix} \frac{1}{8} & \frac{1}{2} & \frac{3}{8} \\ \frac{1}{2} & \frac{1}{2} & 0 \\ \frac{3}{4} & 0 & \frac{1}{4} \end{bmatrix}. \tag{A8}$$

The matrix $U^{(\mathrm{fold})}$ is regular and can be inverted. Its inversion yields a matrix

$$V_{mm'}^{(\mathrm{fold})}=\begin{bmatrix} -\frac{2}{3} & \frac{2}{3} & 1 \\ \frac{2}{3} & \frac{4}{3} & -1 \\ 2 & -2 & 1 \end{bmatrix}, \tag{A9}$$

which transforms the m-resolved DOS from the local reference frame to the global reference frame:

$$n_m^{(\mathrm{glo})}(E)=\sum_{m'=-2}^{0}V_{mm'}^{(\mathrm{fold})}n_{m'}^{(\mathrm{loc})}(E),\quad m=-2,-1,0.$$

If we assume that the m-resolved DOS is independent of the sign of m not only in the global frame but also in the local frame,

$$n_{|m|}^{(\mathrm{loc})}=n_{-|m|}^{(\mathrm{loc})}$$

[consistently with the fact that the matrix U in Eq. (A5) is symmetric], we can unfold the 3×3 matrix $V^{(\mathrm{fold})}$ to a full 5×5 matrix V,

$$V_{mm'}=\begin{bmatrix} -\frac{1}{3} & \frac{1}{3} & 1 & \frac{1}{3} & -\frac{1}{3} \\ \frac{1}{3} & \frac{2}{3} & -1 & \frac{2}{3} & \frac{1}{3} \\ 1 & -1 & 1 & -1 & 1 \\ \frac{1}{3} & \frac{2}{3} & -1 & \frac{2}{3} & \frac{1}{3} \\ -\frac{1}{3} & \frac{1}{3} & 1 & \frac{1}{3} & -\frac{1}{3} \end{bmatrix}, \tag{A10}$$

to get a complete transformation of the m-resolved DOS from the local reference frame to the global reference frame:

$$n_m^{(\mathrm{glo})}(E)=\sum_{m'=-2}^{2}V_{mm'}n_{m'}^{(\mathrm{loc})}(E),\quad m=-2,\ldots,2. \tag{A11}$$

From the way the transformation Eq. (A11) was derived, it follows that it can be used only if the m-resolved DOS for the $+|m|$ states is the same as the DOS for the "$-|m|$

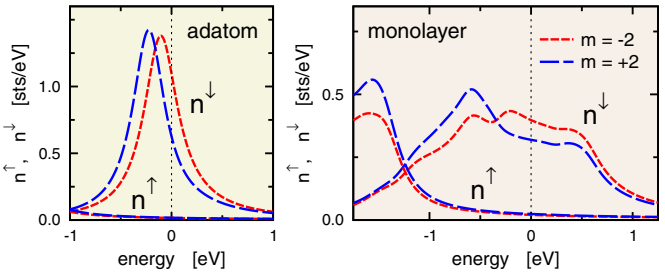

FIG. 8. The $m = -2$ and 2 components of the majority- and minority-spin DOS for a Co adatom and a Co monolayer on Au(111). Magnetization is out-of-plane. Data for majority-spin DOS are labeled by $n^{\uparrow}$, data for minority-spin DOS by $n^{\downarrow}$.

states." As a whole, this is not the case because the SOC splits the "$\pm|m|$ states." Therefore, one cannot simply apply the transformation (A11) to the minority-spin DOS m-resolved in the local reference frame to get the minority-spin DOS m-resolved in the global reference frame: the minority-spin $\pm|m|$ states are split by the SOC, therefore the folding of Eqs. (A4)–(A7) cannot be done and the unfolding of the matrix (A9) to a full matrix (A10) cannot be done either. However, in the energy region in which we are interested, i.e., in the region where the minority-spin states dominate, there is only a little SOC-induced splitting of the $\pm|m|$ states for the *majority spin*. This can be checked explicitly by looking on the m-resolved majority-spin DOS curves in the energy region around Fermi level. As an example, we show here the $m = -2$ and $+2$ DOS components for a Co adatom and a Co monolayer (Fig. 8). We select the case for $\boldsymbol{M}\|\hat{\boldsymbol{z}}$, where the SOC-induced splitting is the largest. One can see that indeed the splitting of the majority-spin DOS (labeled by $n^{\uparrow}$) around E_F is much less than the splitting of the minority-spin DOS (labeled by $n^{\downarrow}$). So even though the transformation (A11) cannot be applied to the minority-spin DOS, it can be applied to the majority-spin DOS.

The m-resolved minority-spin DOS in the global reference frame can thus be recovered in the following way: First, let us evaluate the m-resolved DOS directly in the global reference frame, as indicated in Eq. (A2). Both global spin channels are strongly mixed for in-plane magnetization, so there is only a very small difference between "spin-up" and "spin-down" m-resolved DOS components; if there is no SOC, even this difference disappears. By adding contributions from both spin channels, we get a "total" m-resolved DOS in a global frame, with spin components unresolved. In a second step, we take the m-resolved DOS in the local (rotated) reference frame, keep only its majority-spin component, and transform it to the global reference frame via Eq. (A11). This provides us with a well-defined majority-spin m-resolved DOS in the global reference frame. Finally, we subtract this majority-spin DOS m-resolved in a global frame from the total m-resolved DOS obtained in the first step. This leaves us with minority-spin m-resolved DOS in a basis defined in the global reference frame. This detour (getting minority-spin DOS by subtracting majority-spin DOS from the total DOS) provides more accurate values than what would be obtained if the transformation (A11) was applied to the minority-spin DOS, because the condition (A6) is satisfied much better for the majority-spin states than for the minority-spin states in the energy region of interest.

The procedure described in this appendix should be used only for systems in which there is a substantial exchange splitting between the majority-spin and minority-spin states. Only then can one neglect the SOC-induced $\pm|m|$ splitting of the majority-spin states with respect to the splitting of the minority-spin states (for energies where the minority-spin DOS is much larger than the majority-spin DOS). As an indicative parameter for whether the procedure can be applied or not, we suggest the ratio between the exchange splitting $E_{\downarrow}$-$E_{\uparrow}$ and the SOC constant ξ. Using the parameters given in Table IV, one gets the following values for the $(E_{\downarrow} - E_{\uparrow})/\xi$ ratio: 43.2 for the Fe adatom, 23.1 for the Co adatom, and 5.3 for the Ni adatom. This illustrates why our procedure works nicely for Fe and Co but not so well for Ni, as acknowledged in Sec. III B.

APPENDIX B: DOS FOR $\boldsymbol{M}\|\hat{\boldsymbol{x}}$ RESOLVED IN A LOCAL REFERENCE FRAME

The DOS presented in Sec. III B was resolved according to the magnetic quantum number m in a global reference frame, with the z axis perpendicular to the surface. This ensured the same meaning of the m components no matter how the magnetization is oriented. However, one had to apply an additional procedure described in Appendix A to resolve the spin components. As this procedure assumes that SOC does not split the majority-spin DOS, which is not quite the case here (especially for systems with low exchange splitting such as Ni adatoms and monolayers), one might wonder whether the conclusions based on Figs. 3–5 can be trusted.

Therefore, we present in this appendix the m-resolved DOS for $\boldsymbol{M}\|\hat{\boldsymbol{x}}$ where the magnetic quantum number m refers to a local reference frame, with the spin quantization axis

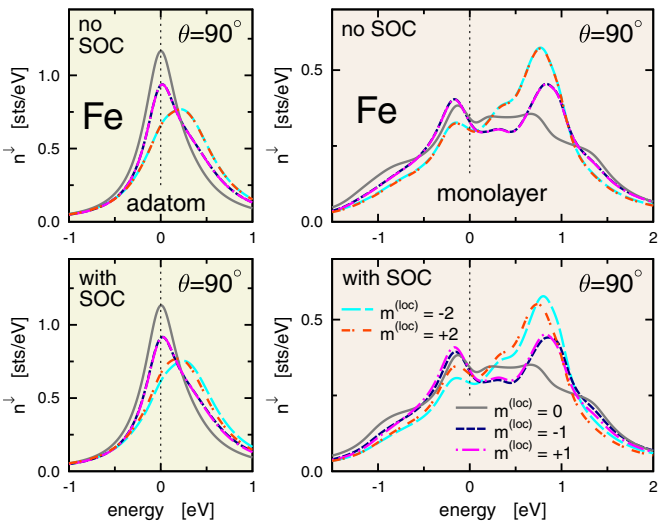

FIG. 9. The d component of the minority-spin DOS for a Fe adatom (left) and a Fe monolayer (right) on Au(111) for magnetization parallel to the surface, with SOC either ignored (top) or included (bottom). The DOS is resolved according to the magnetic quantum number m in a local reference frame where the $z^{(\mathrm{loc})}$ axis is parallel to the Au(111) surface.

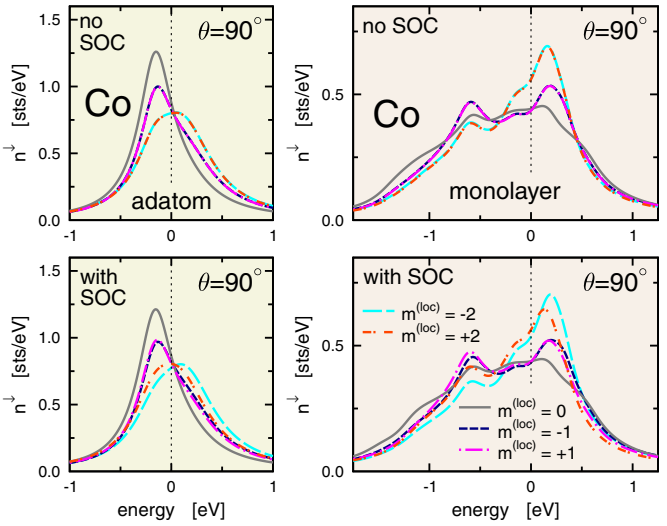

FIG. 10. The d component of the minority-spin DOS for a Co adatom (left) and a Co monolayer (right) on Au(111) for magnetization parallel to the surface. This figure is analogous to Fig. 9.

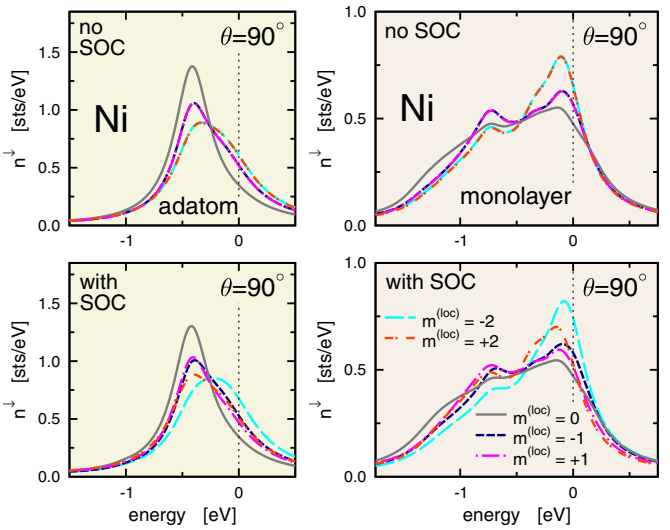

FIG. 11. The d component of the minority-spin DOS for a Ni adatom (left) and a Ni monolayer (right) on Au(111) for magnetization parallel to the surface. This figure is analogous to Fig. 9.

$z^{(\mathrm{loc})}$ parallel to $\boldsymbol{M}$. The outcome is presented in Figs. 9–11. Analogous plots for $\boldsymbol{M} \| \hat{\boldsymbol{z}}$ would be the same as respective panels in Figs. 3–5, because in such a case the local and global reference frames coincide. Note that the individual m-components presented in Figs. 9–11 cannot be directly compared to analogous components in Figs. 3–5 because their definitions differ. This can be clearly seen when comparing the DOS for systems without SOC, when there can be in principle no dependence on the magnetization direction. The graphs in the panels that are second from the top in Figs. 3–5 and in the top panels of Figs. 9–11 describe the same physical situation and yet the individual curves differ—because the magnetic quantum numbers are defined with respect to different reference frames.

Even though the m components are defined differently, one can still qualitatively compare how SOC affects the DOS for $\theta = 0^\circ$ and for $\theta = 90^\circ$. Concerning the situation for $\theta = 0^\circ$, one monitors in Figs. 3–5 how the plot without SOC changes if SOC is switched on (i.e., one looks at the two middle panels of the corresponding figure). Concerning the situation for $\theta = 90^\circ$, one monitors analogous changes in Figs. 9–11. One can clearly see that the effect of SOC is much more pronounced for $\theta = 0^\circ$ than for $\theta = 90^\circ$. This confirms and strengthens the conclusions drawn in Sec. III B, where the emphasis was put rather on maintaining the possibility for a component-by-component comparison than on formal correctness.

[1] H. J. F. Jansen, Phys. Rev. B **38**, 8022 (1988).
[2] S. Bornemann, J. Minár, J. Braun, D. Koedderitzsch, and H. Ebert, Solid State Commun. **152**, 85 (2012).
[3] P. Ravindran, A. Kjekshus, H. Fjellvåg, P. James, L. Nordström, B. Johansson, and O. Eriksson, Phys. Rev. B **63**, 144409 (2001).
[4] H. J. F. Jansen, G. S. Schneider, and H. Y. Wang, in *Electronic Structure and Magnetism of Complex Materials*, Springer Series in Materials Science Vol. **5**4, edited by J. Singh and D. A. Papaconstantopoulos (Springer, Berlin, 2003), p. 57.
[5] O. Šipr, S. Bornemann, J. Minár, and H. Ebert, Phys. Rev. B **82**, 174414 (2010).
[6] O. Šipr, S. Bornemann, H. Ebert, and J. Minár, J. Phys.: Condens. Matter **26**, 196002 (2014).
[7] P. Bruno, Phys. Rev. B **39**, 865 (1989).
[8] G. van der Laan, J. Phys.: Condens. Matter **10**, 3239 (1998).
[9] G. Autès, C. Barreteau, D. Spanjaard, and M.-C. Desjonquères, J. Phys.: Condens. Matter **18**, 6785 (2006).
[10] T. Kosugi, T. Miyake, and S. Ishibashi, J. Phys. Soc. Jpn. **83**, 044707 (2014).
[11] L. Ke and M. van Schilfgaarde, Phys. Rev. B **92**, 014423 (2015).
[12] D. S. Wang, R. Wu, and A. J. Freeman, Phys. Rev. B **48**, 15886 (1993).
[13] A. Lessard, T. H. Moos, and W. Hübner, Phys. Rev. B **56**, 2594 (1997).
[14] F. Gimbert and L. Calmels, Phys. Rev. B **86**, 184407 (2012).
[15] D. S. Wang, R. Wu, and A. J. Freeman, Phys. Rev. B **47**, 14932 (1993).
[16] G. H. O. Daalderop, P. J. Kelly, and M. F. H. Schuurmans, Phys. Rev. B **50**, 9989 (1994).
[17] T. H. Moos, W. Hübner, and K. H. Bennemann, Solid State Commun. **98**, 639 (1996).
[18] S. Blügel, in *30. Ferienkurs des Instituts für Festkörperforschung 1999 "Magnetische Schichtsysteme,"*edited by R. Hölzle (Forschungszentrum Jülich, Jülich, 1999), p. C1.1.
[19] T. O. Strandberg, C. M. Canali, and A. H. MacDonald, Nat. Mater. **6**, 648 (2007).
[20] V. Antropov, L. Ke, and D. Aberg, Solid State Commun. **194**, 35 (2014).

[21] I. G. Rau, S. Baumann, S. Rusponi, F. Donati, S. Stepanow, L. Gragnaniello, J. Dreiser, C. Piamonteze, F. Nolting, S. Gangopadhyay, O. R. Albertini, R. M. Macfarlane, C. P. Lutz, B. A. Jones, P. Gambardella, A. J. Heinrich, and H. Brune, Science **344**, 988 (2014).
[22] A. A. Khajetoorians and J. Wiebe, Science **344**, 976 (2014).
[23] S. Baumann, F. Donati, S. Stepanow, S. Rusponi, W. Paul, S. Gangopadhyay, I. G. Rau, G. E. Pacchioni, L. Gragnaniello, M. Pivetta, J. Dreiser, C. Piamonteze, C. P. Lutz, R. M. Macfarlane, B. A. Jones, P. Gambardella, A. J. Heinrich, and H. Brune, Phys. Rev. Lett. **115**, 237202 (2015).
[24] S. Bornemann, O. Šipr, S. Mankovsky, S. Polesya, J. B. Staunton, W. Wurth, H. Ebert, and J. Minár, Phys. Rev. B **86**, 104436 (2012).
[25] S. H. Vosko, L. Wilk, and M. Nusair, Can. J. Phys. **58**, 1200 (1980).
[26] H. Ebert, D. Ködderitzsch, and J. Minár, Rep. Prog. Phys. **74**, 096501 (2011).
[27] H. Ebert, *The SPRKKR package version 7*, http://olymp.cup.uni-muenchen.de/ak/ebert/SPRKKR (2014).
[28] J. Minár, S. Bornemann, O. Šipr, S. Polesya, and H. Ebert, Appl. Phys. A **82**, 139 (2006).
[29] H. Ebert, H. Freyer, A. Vernes, and G.-Y. Guo, Phys. Rev. B **53**, 7721 (1996).
[30] G. Kresse and J. Hafner, Phys. Rev. B **47**, 558 (1993).
[31] G. Kresse, M. Marsman, and J. Furthmüller, *The VASP package*, https://www.vasp.at (2014).
[32] I. B. Bersuker, *Electronic Structure and Properties of Transition Metal Compounds: Introduction to the Theory* (Wiley, Hoboken, NJ, 2010).
[33] J. Stöhr and H. C. Siegmann, *Magnetism: From Fundamentals to Nanoscale Dynamics* (Springer, Berlin, 2006).
[34] J. W. Davenport, R. E. Watson, and M. Weinert, Phys. Rev. B **37**, 9985 (1988).
[35] P. Weinberger, *Magnetic Anisotropies in Nanostructured Matter* (CRC, Boca Raton, FL, 2008).
[36] X. D. Wang, R. Wu, D. S. Wang, and A. J. Freeman, Phys. Rev. B **54**, 61 (1996).
[37] J. B. Staunton, L. Szunyogh, A. Buruzs, B. L. Gyorffy, S. Ostanin, and L. Udvardi, Phys. Rev. B **74**, 144411 (2006).
[38] F. Donati, Q. Dubout, G. Autès, F. Patthey, F. Calleja, P. Gambardella, O. V. Yazyev, and H. Brune, Phys. Rev. Lett. **111**, 236801 (2013).
[39] F. Donati, A. Singha, S. Stepanow, C. Wäckerlin, J. Dreiser, P. Gambardella, S. Rusponi, and H. Brune, Phys. Rev. Lett. **113**, 237201 (2014).
[40] A. Jesche, R. W. McCallum, S. Thimmaiah, J. L. Jacobs, V. Taufour, A. Kreyssig, R. S. Houk, S. L. Bud´ko, and P. C. Canfield, Nat. Commun. **5**, 3333 (2014).
[41] P. Novák and F. R. Wagner, Phys. Rev. B **66**, 184434 (2002).
[42] V. P. Antropov and V. N. Antonov, Phys. Rev. B **90**, 094406 (2014).
[43] B. Újfalussy, L. Szunyogh, P. Bruno, and P. Weinberger, Phys. Rev. Lett. **77**, 1805 (1996).
[44] G. Lugert, W. Robl, L. Pfau, M. Brockmann, and G. Bayreuther, J. Magn. Magn. Mater. **121**, 498 (1993).
[45] O. Toulemonde, V. Petrov, A. Nait Abdi, and J. P. Bucher, J. Appl. Phys. **95**, 6565 (2004).
[46] W. C. Lin, H. Y. Chang, Y. C. Hu, and C. C. Kuo, IEEE Trans. Magn. **45**, 4037 (2009).
[47] T. Allmers and M. Donath, Phys. Rev. B **81**, 064405 (2010).
[48] H. A. Dürr, S. S. Dhesi, E. Dudzik, D. Knabben, G. van der Laan, J. B. Goedkoop, and F. U. Hillebrecht, Phys. Rev. B **59**, R701 (1999).
[49] G. Rodary, V. Repain, R. L. Stamps, Y. Girard, S. Rohart, A. Tejeda, and S. Rousset, Phys. Rev. B **75**, 184415 (2007).
[50] N. Tournerie, A. Engelhardt, F. Maroun, and P. Allongue, Surf. Sci. **631**, 88 (2015).
[51] S. Padovani, F. Scheurer, I. Chado, and J. P. Bucher, Phys. Rev. B **61**, 72 (2000).
[52] J. Stöhr and H. König, Phys. Rev. Lett. **75**, 3748 (1995).
[53] J. Stöhr, J. Magn. Magn. Mater. **200**, 470 (1999).
[54] M. E. Rose, *Elementary Theory of Angular Momentum* (Wiley, New York, 1957).